Key Points:

- 27-day signatures are extracted from ionospheric N_e and n_{O_2} via superposed epoch analysis and a lag analysis is applied
- The height-dependent delay of the extracted 27-day signatures is characterized by major absorption processes of O and O_2
- Good correlations between observed delays of N_e and n_{O_2} confirm modeling results in preceding studies

Correspondence to:

E. Schmölter,
Erik.Schmoelter@dlr.de

Solar Activity Driven 27-Day Signatures in Ionospheric Electron and Molecular Oxygen Densities

Erik Schmölter[1] and **Christian von Savigny[2]**

[1]Institute for Solar-Terrestrial Physics, German Aerospace Center, Neustrelitz, Germany, [2]Institute of Physics, University of Greifswald, Greifswald, Germany

Abstract The complex interactions in the upper atmosphere, which control the height-dependent ionospheric response to the 27-day solar rotation period, are investigated with the superposed epoch analysis technique. 27-day signatures describing solar activity are calculated from a solar proxy (F10.7) and wavelength-dependent extreme ultraviolet (EUV) fluxes (Thermosphere Ionosphere Mesosphere Energetics and Dynamics/Solar EUV Experiment), and the corresponding 27-day signatures describing ionospheric conditions are calculated from electron density profiles (Pruhonice ionosonde station) and O_2 density profiles (Global-scale Observations of the Limb and Disk). The lag analysis of these extracted signatures is applied to characterize the delayed ionospheric response at heights from 100 to 300 km and the impact of major absorption processes in the lower (dominated by O_2) and upper ionosphere (dominated by O) is discussed. The observed variations of the delay in these regions are in good agreement with model simulations in preceding studies. Additionally, the estimated significance and the correlation of the delays based on both ionospheric parameters are good. Thus, variations such as the strong shift in 27-day signatures for the O_2 density at low heights are also reliably identified (up to half a cycle). The analysis confirms the importance of ionospheric and thermospheric coupling to understand the variability of the delayed ionospheric response and introduces a method that could be applied to additional ionosonde stations in future studies. This would allow to describe the variability of the delayed ionospheric response spatially, vertically and temporally and therefore may contribute further to the understanding of processes and improve ionospheric modeling.

1. Introduction

Solar extreme ultraviolet (EUV) radiation is absorbed in different ionization and dissociation processes in the upper atmosphere driving the creation of the ionospheric plasma. The composition of this plasma is significantly affected by variations of the solar activity but geomagnetic (driven by the solar wind) and meteorological variability contribute to ionospheric variability as well (Rishbeth & Mendillo, 2001). Thus, changes of the plasma occur on different spatial and temporal scales, which may further depend on additional parameters (e.g., solar zenith angle). Nevertheless, significant signatures in the ionospheric plasma are related to corresponding changes in the solar EUV radiation. The 27-day solar rotation period (appearance and disappearance of active regions on the solar disc) causes continuous variations of the solar EUV spectrum which in turn cause observable 27-day signatures for different ionospheric parameters (Ma et al., 2012).

Photoionization of O to O^+ at heights from 150 to 500 km defines the so-called F region with the maximum of the plasma density profile. The amount of O^+ dominates the ionospheric plasma in this region. Photoionization of O_2 to O_2^+ and photodissociation of O_2 to O at heights from 90 to 150 km (as well as further absorption processes or charge exchange) cause a different plasma composition in the lower ionosphere. Additionally, recombination processes occur depending on the existing plasma composition at different heights (Kelley, 2009). The 27-day signatures, which are driven by the solar EUV radiation, thus also show height-dependent variations based on the contribution of the different processes (Schmölter et al., 2022).

In the upper ionosphere the 27-day signatures of the plasma density are controlled by production and loss of O^+ (Ren et al., 2018; Schmölter et al., 2022). The production due to photoionization of O is almost immediate and increased due to the photodissociation of O_2 and upward transport processes during the time of increasing solar activity (first phase of 27-day solar rotation period). The recombination is not immediate and therefore an accumulation of O^+ may occur resulting in an observable time difference between the solar and ionospheric 27-day signatures (Schmölter et al., 2022). This delayed ionospheric response and its variability has been characterized

for different solar and ionospheric measurements (Afraimovich et al., 2008; Jakowski et al., 1991, 2002; Lee et al., 2012; Min et al., 2009; Oinats et al., 2008; Ren et al., 2018; Schmölter et al., 2018, 2020; Titheridge, 1973; Zhang & Holt, 2008) and simulations qualified and quantified the impact of different processes driving temporal and spatial variations (Ren et al., 2018, 2019, 2020; Schmölter et al., 2021; Vaishnav et al., 2018, 2019, 2021).

Schmölter et al. (2022) investigated the height-dependent variations of the delayed ionospheric response via a case study using electron density profiles calculated from ionosonde measurements (station Grahamstown). Additionally, Thermosphere-Ionosphere-Electrodynamics General Circulation Model (TIE-GCM) simulations were performed to investigate the interaction of ionospheric processes. The investigated electron density profiles from 27 April 2019 to 24 May 2019 were correlated with solar and weak geomagnetic activity. In addition, a good agreement was found with the thermospheric response during that period reported by Cai et al. (2021). Schmölter et al. (2022) confirmed the almost immediate response to the 27-day solar rotation at the electron density peak. The 27-day signatures at lower heights could only be analyzed to a limited extent due to the lower correlation with solar activity, but a larger shift of the 27-day signature was indicated. Schmölter et al. (2022) further discussed the superposed epoch analysis (SEA) technique (also known as composite analysis) for the 27-day signature in foF2 and hmF2 calculated from the ionosonde measurements. This approach was described in different studies (e.g., von Savigny et al., 2019; Rong et al., 2020) and allowed to calculate statistically significant 27-day signatures for the two F2 layer specific parameters.

In the present study the analysis of the height-dependent delayed ionospheric response is extended based on the suggestions by Schmölter et al. (2022). Rather than for selected ionospheric parameters calculated from ionosonde measurements, an analysis of the electron density at different heights is performed. This approach allows to extract statistically significant 27-day signatures at all investigated heights and therefore the characterization of the delayed ionospheric response in the lower ionosphere. Further, the analysis is extended by applying wavelength-dependent solar irradiance measurements by the Solar EUV Experiment (SEE) on the Thermosphere Ionosphere Mesosphere Energetics and Dynamics (TIMED) satellite mission. The resulting wavelength- and height-dependent 27-day signatures (and delays) indicate in detail the contribution of different processes and major species. Finally, the SEA technique is also applied to O_2 density measurements by the Global-scale Observations of the Limb and Disk (GOLD) on the SES-14 satellite mission.

The resulting 27-day signatures of electron and O_2 density confirm the role of photoionization and photodissociation in regard to the delayed ionospheric response as established in previous studies (e.g., Jakowski et al., 1991; Ren et al., 2018; Schmölter et al., 2021) and allow the discussion of features calculated from measurement data for the whole ionosphere.

2. Data

The analysis in the present study requires solar and ionospheric/thermospheric measurements to calculate the delayed ionospheric response using the SEA approach. The data must be available for long periods (several years) to select a significant number of 27-day solar rotation periods. In addition, a small number of large data gaps (several days) in the selected periods is required to successfully extract 27-day signatures. This requirement is generally satisfied by solar EUV proxies and measurements, but has to be considered for different upper atmosphere height profile data sets.

2.1. Solar Radio Flux Index F10.7

F10.7, which is a measurement of the solar radiation at a wavelength of 10.7 cm, is well-suited to describe the total solar activity and is often applied as a proxy for solar radiation at different wavelengths (Tapping, 2013). For these reasons, F10.7 was used in several studies (e.g., Afraimovich et al., 2008; Jakowski et al., 1991; Jakowski et al., 2002; Lee et al., 2012; Min et al., 2009; Oinats et al., 2008; Schmölter et al., 2021; Zhang & Holt, 2008) to calculate the delayed ionospheric response and is also applied in the present study to identify significant 27-day signatures in the solar activity.

The National Aeronautics and Space Administration (NASA) Goddard Space Flight Center's (GSFC) OMNI data set includes F10.7 data, which are provided through the OMNIWeb interface (NASA, 2022b).

2.2. TIMED/SEE Solar Irradiance Measurements

The SEE on the TIMED satellite mission measures the solar irradiance for approximately 3 min each 97-min orbit (Woods, 2005; Woods et al., 1998, 2000). The Extreme-Ultraviolet Grating Spectrograph (EGS) measures

the solar irradiance from 26 to 190 nm and the X-Ray-Ultraviolet Photometer System (XPS) measures the solar irradiance from 0.1 to 35 nm and at 121.5 nm (Woods, 2005). In the present study SEE level 3 data are applied, which contain a joined solar irradiance spectrum with intervals of 1 nm. This spectrum is derived from EGS and XPS level 2 data. The estimated accuracy for the SEE measurements is 10%–20% (Woods, 2005).

The different SEE data sets are provided by the Laboratory for Atmospheric and Space Physics (LASP) via the SEE home page (LASP, 2022).

2.3. Ionosonde Electron Density Profiles

In the present study a mid-latitude station is selected from the Master Ionosonde Data Set (MIDS) by considering the data coverage (several years with a minimum of data gaps). For this reason, the station Prohunice (50.0°N and 14.6°E), which provides ionosonde data since 2004, is appropriate and applied in the analysis.

The ionograms, which include calculated electron density profiles, are generated from measured tracings of reflected high frequency radio pulses. These traces may in some cases be unreliable or wrong resulting in electron density profiles that are not suitable for the analysis. A manual detection and exclusion of these wrong traces is not feasible for long periods (at sampling rate of 15 min), but instead the Assigned Quality Index (AQI) is evaluated to reduce the impact of unreliable data. Thus, electron density profiles are only included in the analysis if the corresponding AQI is greater than 1 (good and very good data). Additionally, the SEA technique is expected to reduce the impact of remaining deviations. The electron densities at different heights are not measured independently of each other and thus a correlation with each other is expected. This may in turn influence a lag analysis and must therefore also be investigated in detail.

Real time ionograms and archived data sets are provided by the National Oceanic and Atmospheric Administration's (NOAA) National Centers for Environmental Information (NCEI) via a web interface (NCEI, 2022). Real time data of the ionospheric station Prohunice are also provided through the Institute of Atmospheric Physics of the Czech Academy of Sciences (CAS) web interface (CAS, 2022).

2.4. GOLD O_2 Density Profiles

The GOLD performs approximately 10 occultation measurements each day sampling from a set of 30 stars on the east and west limbs relative to the fixed satellite position (Eastes et al., 2017, 2020; Lumpe et al., 2020). The O_2 density profiles are calculated from these measurements in the Schumann-Runge continuum (from 134 to 162 nm), which are mapped to a 2-dimensional representation (tangent height and wavelength) of the signal. These profiles are then further processed using the algorithm described in detail by Lumpe et al. (2020) to estimate height-dependent O_2 density profiles. O_2 density measurements are generally provided at heights from 120 to 240 km on a vertical grid with sampling rate of 5 km. The accuracy is estimated as 10% (Lumpe et al., 2020).

The GOLD O_2 density data and further GOLD data sets are provided by NASA via the GOLD Science Data Center (NASA, 2022a).

2.5. GOLD N_2 LBH Radiance

Additionally, GOLD performs daytime disk scan measurements, which are applied to calculate the column abundance of thermospheric O relative to N_2 (Eastes et al., 2017, 2020; Lumpe et al., 2020). The O/N_2 column densities are calculated from OI 135.6 nm and N_2 Lyman-Birge-Hopfield (LBH) dayglow according to the algorithm by Strickland et al. (1995). While the retrieved O/N_2 column densities have been applied in previous studies to discuss the delayed ionospheric response (Schmölter et al., 2021), the present study uses only the N_2 LBH radiance. This allows a comparison of the O_2 and N_2 measurements.

The GOLD O/N_2 data are also provided by NASA via the GOLD Science Data Center (NASA, 2022a).

3. Height-Dependent Lag Analysis of Electron Density Profiles

Schmölter et al. (2022) applied the SEA technique to extract a solar 27-day signature in foF2 and hmF2 time series. This approach, which is described in detail in other studies (e.g., von Savigny et al., 2019; Rong et al., 2020), is
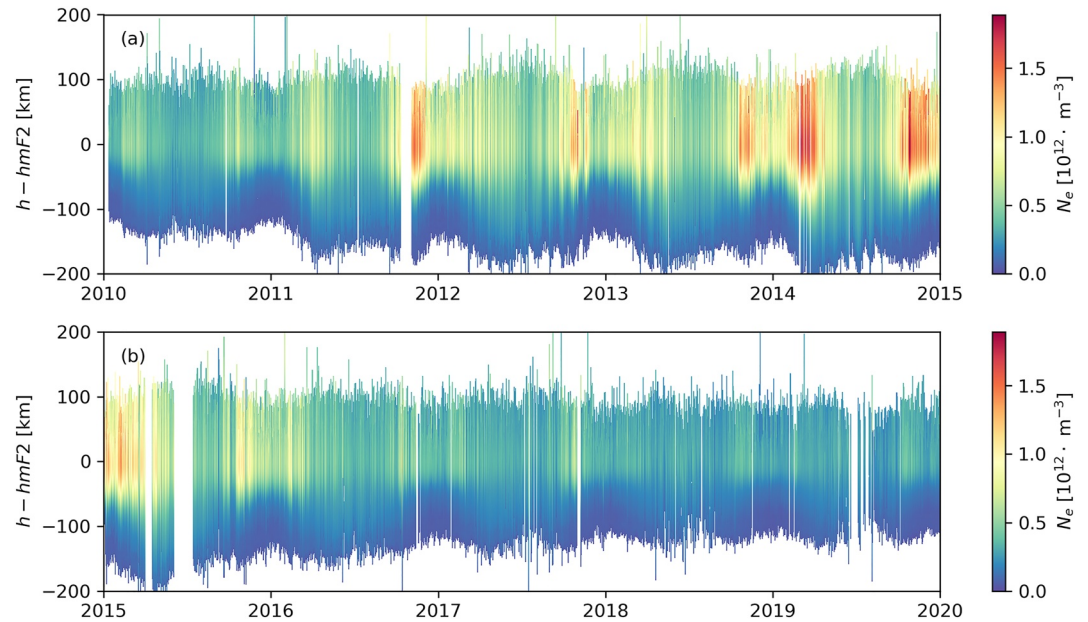
Figure 1. Electron density N_e profiles (daily mean between 9:00LT and 15:00LT) from 2010 to 2020 (a and b) for station Prohunice (50.0°N and 14.6°E) at relative heights. The reference heights are the peak heights (hmF2) of each N_e profile.

extended to analyze the electron density N_e at different heights. For this purpose, relative heights are introduced that are calculated for each N_e profile based on the absolute height h and the heights of the N_e peak as

$$h_r(t) = h(t) - hmF2(t). \tag{1}$$

The N_e peak height is assumed to be the same as the peak height of the F2 layer hmF2, since the station Prohunice is a mid-latitude location and thus E region dominated ionospheric conditions are expected to have no significant impact (Kamal et al., 2020). The resulting N_e profiles (daily mean between 9:00LT and 15:00LT) from 2010 to 2019 are shown in Figure 1. There are longer data gaps in 2011 and 2015 but the data coverage is generally good and several smaller gaps may be interpolated if these periods are selected for the SEA approach. Throughout the whole period there are outliers (increase or decrease of N_e at unexpected heights), which may be attributed to wrong traces, artifacts or variations in the lower ionosphere (E region dominated ionosphere). These deviations have no significant impact on the further analysis and for that reason the chosen AQI requirement is considered sufficient to assure reliable data.

The N_e profiles are correlated well with the 11-year solar cycle (SC). The ascending phase up to the solar maximum of SC 24 is represented in Figure 1a and the descending phase up to the solar minimum is represented in Figure 1b. The strongest increases are observed in 2014 and 2015. The extent of the N_e profiles also follows the 11-year SC limiting the height range that is selected for the further analysis to relative heights from −100 to 50 km. This height range covers the regions with the major contributions of O^+ and O_2^+ to the plasma density profile (and thus N_e profile) though and is therefore sufficient. Since the calculation of the N_e profile is only performed up to hmF2 without additional assumptions, the analysis is further restricted to heights from −100 to 20 km. A range of 20 km above the peak is included nonetheless to identify the F2 peak.

The calculation of superimposed epochs is prepared by estimating anomaly time series of F10.7 and $N_e(h_r)$ series. The anomaly time series are calculated by subtracting a 35-day moving average from the original time series and applying a 5-day moving average for smoothing. The resulting F10.7 anomalies are shown in Figure 2. The SC variation in the period from 2010 to 2019 is again represented and the strong N_e increases in 2014 and 2015 (see Figure 1) are related to strong anomalies as well. The epoch centers, that are used to calculate the epoch average anomalies, are shown with the black dots in Figure 2. These epoch centers are F10.7 maxima with an enhanced solar activity (greater than 7.5 sfu). N_e anomaly time series are extracted for each relative height from −100 to 20 km as well.

Next, periods of 54 days are extracted from the anomaly time series for each of the estimated epoch centers resulting in matrices for F10.7 and all selected $N_e(h_r)$. The column-wise mean of these matrices produces the
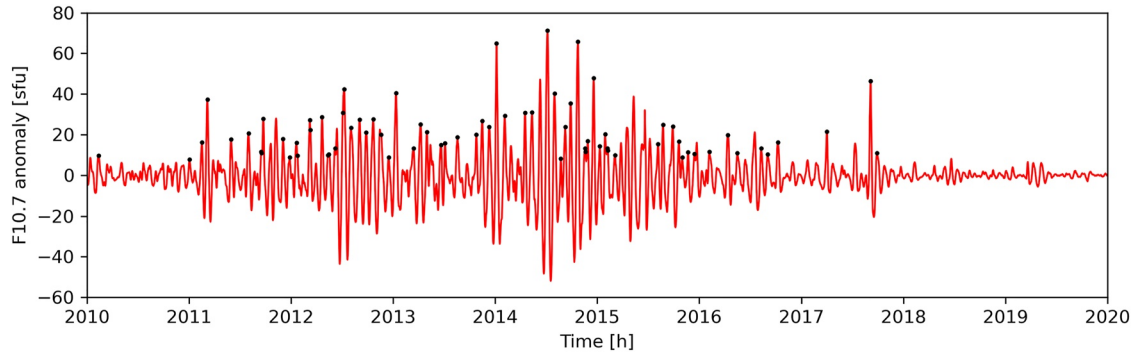
Figure 2. Anomaly time series of F10.7 (red line) from 2010 to 2020. The identified F10.7 maxima (i.e., the epoch centers) are shown as black dots. Only F10.7 maxima greater than 7.5 sfu are included.

epoch averaged anomalies, which show well-defined 27-day signatures for F10.7 and $N_e(-30$ km) in Figure 3. Both epoch averaged anomalies are correlated and a constant delay of approximately 2 days is observed. The epoch averaged $N_e(-30$ km) anomaly shows small variations, but generally both time series reflect a well-defined 27-day signature (see sinusoidal fit in Figure 3).

The significance of the results is estimated using the Monte-Carlo approach, that was applied in previous studies (von Savigny et al., 2019; Schmölter et al., 2022). For this purpose, the SEA procedure is repeated for 1,000 random selections of epoch centers and for each result the 27-day sinusoidal fit is calculated (see gray lines in Figure 3). The fraction of amplitudes of these sinusoidal fits, that exceed the sinusoidal fit amplitude of the epoch averaged $N_e(-30$ km) anomaly, are estimated to retrieve a measure for the significance. The results in Figure 3 show a small fraction of 0.10% (fraction converges approximately at this value for even larger sample sizes) and thus the solar activity is likely the driver of the observed variations. The maximum fraction observed is 0.61% at the relative height of −69 km and the mean fraction is 0.19%. For this reason, the results at all relative heights are significant and the whole height range is further analyzed. The fraction of 0.20% for the epoch averaged $N_e(0$ km) anomaly (NmF2 anomaly) is similar to the fraction of 0.40% which Schmölter et al. (2022) estimated for the epoch averaged foF2 anomaly. Thus, despite different stations and time periods, the results are approximately in the same order of significance.
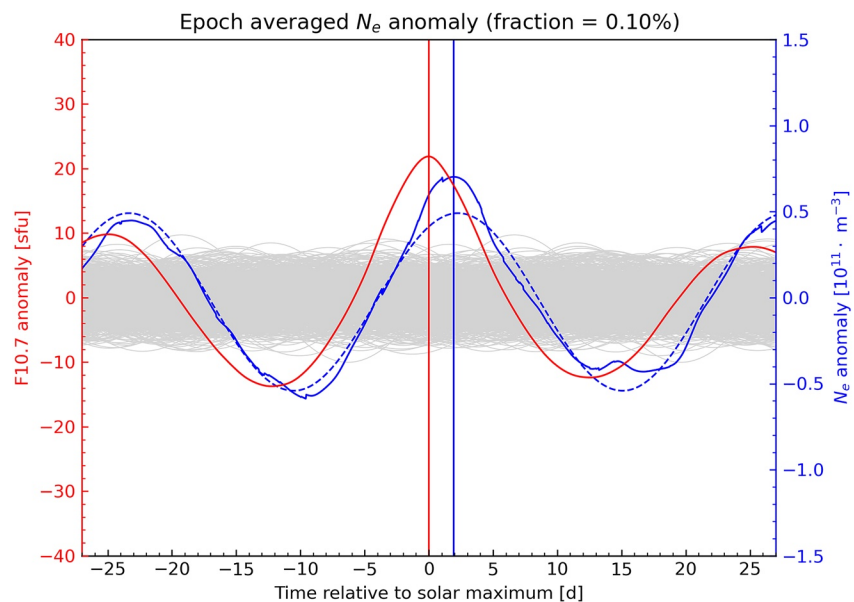

Figure 3. Superposed epoch analysis (SEA) results for F10.7 (red line) and electron density N_e at the relative height of −30 km (blue line). The vertical lines mark the corresponding peak maxima. The dashed blue line shows the sinusoidal fit for the $N_e(-30$ km) SEA. The gray lines are a sample result of the Monte-Carlo significance test for $N_e(-30$ km).
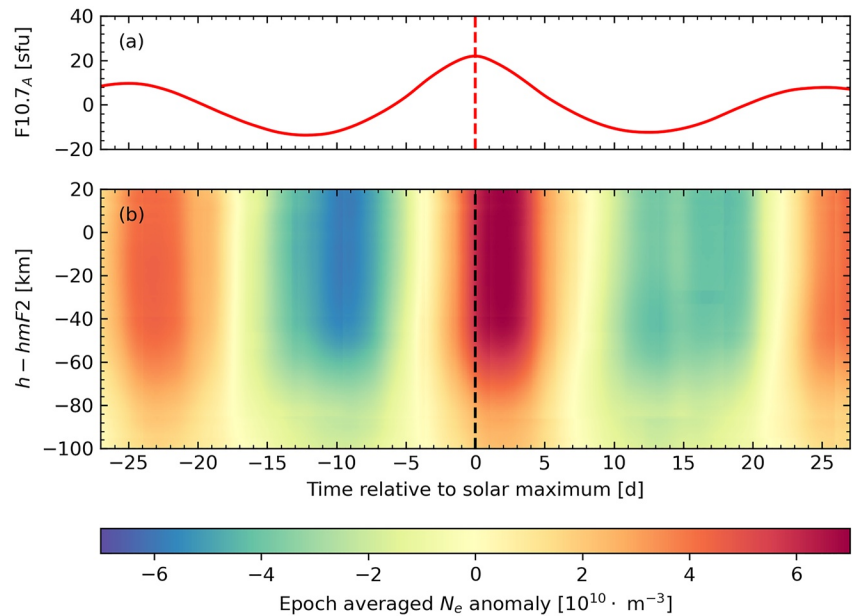
Figure 4. Superposed epoch analysis results for F10.7 (a) and electron density N_e at relative heights from -100 to 20 km (b).

The epoch averaged N_e anomalies at relative heights from -100 to 20 km are shown in Figure 4b. 27-day signatures are observed at all heights but are less pronounced in the lower ionosphere due to the reduced N_e. Figure 4b also indicates variations of the lag at different heights which are calculated using the epoch averaged F10.7 and N_e anomalies.

The lag is estimated with two methods, that were applied in various studies investigating the delayed ionospheric response. The time difference $dt(h_r)$ between peak maximum of F10.7 and $N_e(h_r)$ considers only the maximum response of the ionosphere to solar activity changes. The method is well-suited to describe height-dependent variations (Schmölter et al., 2022) but cannot describe changes that may occur during the ascending and descending phase of the 27-day solar rotation period (e.g., ongoing accumulation). The lag $\tau_{CC}(h_r)$ that is calculated using the cross-correlation of F10.7 and $N_e(h_r)$ evaluates the whole 27-day signature.

Figure 5a shows the delay height profiles that are calculated from the epoch averaged F10.7 and $N_e(h_r)$ anomalies in Figure 4. The τ_{CC} profile (calculated from the epoch averaged F10.7 and N_e anomalies) reflects variations that were reported by Schmölter et al. (2022) in TIE-GCM simulations using an artificial sinusoidal input. The maximum of the delay is observed in the upper ionosphere (approximately at the N_e peak) and related to the accumulation of O^+, which is caused due to the imbalance of production and loss (Ren et al., 2018; Schmölter et al., 2022). The delay decreases at lower heights up to a minimum at approximately -70 km. This minimum of the delay is related to the accumulation of O_2^+, which peaks before the accumulation of O^+ due to the photodissociation of O_2 changing the neutral composition in favor of O (Schmölter et al., 2022). The dt_{max} profile follows the τ_{CC} profile at heights below -40 km, but a mean difference of approximately 6 hr is observed. The dt_{max} maximum at 10 km is strongly pronounced with adjacent decreases at 0 and 20 km. This variation indicates that the accumulation of O^+ is limited to a small height range during the maximum N_e response to the solar 27-day signature.

Figure 5b shows the delays for the same approach but epoch centers of less significant F10.7 anomalies are included. Especially the dt_{max} profile changes due to this adjustment and follows the τ_{CC} profile at all heights. The mean difference between both delays is approximately 8 hr. The difference between the delay profiles with and without less significant F10.7 anomalies are shown in Figure 5c. τ_{CC} is not significantly affected by the adjusted selection, but dt_{max} is increased by several hours at all heights. The strongest changes are observed in the upper ionosphere and at lower heights the difference decreases continuously. The inclusion of more epoch centers with less significant F10.7 and $N_e(h_r)$ anomalies emphasizes the whole 27-day signature stronger than the N_e maximum. This may contribute to the observed similarity of the dt_{max} profile and the τ_{CC} profile for these conditions. The increased delays in Figure 5b compared to Figure 5a may also be attributed to this relation.
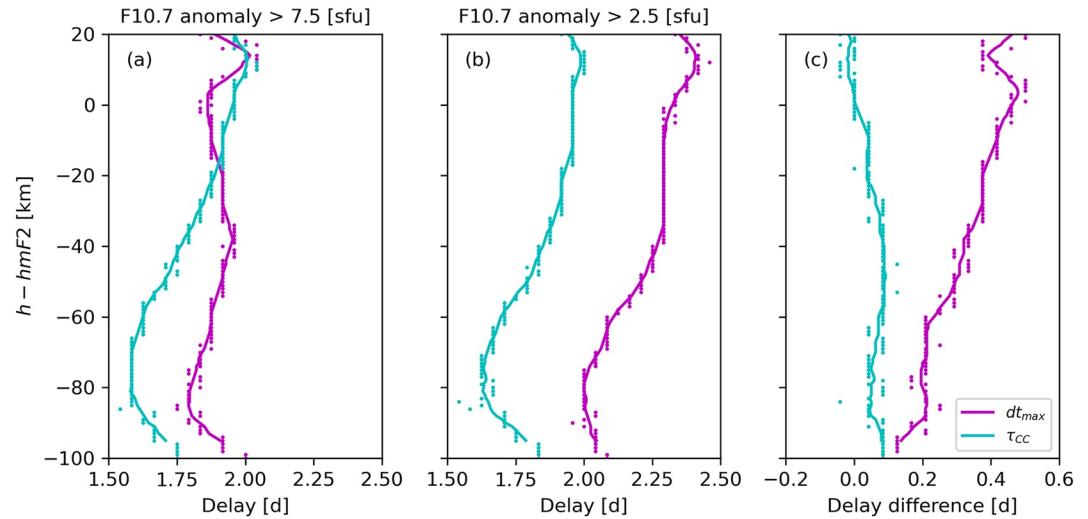
Figure 5. Delay between epoch averaged F10.7 and $N_e(h_r)$ anomalies with epoch centers where the F10.7 anomaly is greater than 7.5 (a) and 2.5 sfu (b). Delays are estimated using the time difference between peak maxima dt_{max} (magenta dots) and the cross-correlation lag τ_{CC} (cyan dots). The corresponding lines show a running mean with a window of 10 km for each data set. The difference between results (c) is shown using the same representation.

The SEA technique applied to N_e time series at relative heights allowed to define statistically significant height profiles for the delayed ionospheric response. Thus the results in Figure 5 are a significant extension of the case study performed by Schmölter et al. (2022). Based on the analysis and the good agreement with previous studies, an additional extension of the approach is performed. The applied solar proxy F10.7 is replaced with the wavelength-dependent EUV spectrum, which provides further insight to the processes driving the delayed ionospheric response.

4. Height- and Wavelength-Dependent Lag Analysis of Electron Density Profiles

The EUV spectrum from 1 to 190 nm is analyzed with the epoch centers estimated based on F10.7 anomalies (see Figure 2) and thus the same periods are analyzed for all solar irradiance time series $S(\lambda)$. This introduces $S(\lambda)$ peaks, which are not centered (lag between F10.7 and $S(\lambda)$ anomalies), but neither dt_{max} nor τ_{CC} are impacted by such a time difference (not centered maximum) and thus the procedure applied to calculate the delayed ionospheric response requires no adjustment. The amplitude of $S(\lambda)$ varies strongly for different wavelengths λ and these variations must be considered to obtain SEA results that can be compared with each other. For this reason, the analysis is performed with the normalized $S(\lambda)$ time series (standard score).

The epoch averaged $S(\lambda)$ anomalies in Figure 6 show well-defined 27-day signatures. There are stronger deviations for greater wavelengths, but generally a sinusoidal variation similar to the epoch averaged F10.7 anomaly is observed (see Figure 3). The most significant difference is the asymmetric amplitude, which is strongly pronounced for wavelengths greater than 150 nm. The epoch averaged $S(\lambda)$ anomalies with wavelengths of the EUV spectrum are not affected. The $S(\lambda)$ anomaly peaks are as expected not centered and positive lags compared to the F10.7 anomaly peak are observed.

Next, the correlation $r(\lambda, h_r)$ and delay $\tau(\lambda, h_r)$ between epoch averaged $S(\lambda)$ and $N_e(h_r)$ are calculated using the same methods that were applied to estimate the delays in Figure 5 from the anomaly time series in Figure 4. The results, which are shown in Figure 7, present the height- and wavelength-dependent delayed ionospheric response.

The correlations Figure 7a are generally good. Moderate correlations are observed at wavelengths greater than 150 nm and relative heights greater than −40 km. This part of the EUV spectrum is not absorbed in the upper ionosphere and therefore lower correlations may be expected. This impact is superposed with the variations introduced due to the deviations and asymmetric amplitude that are observed for the corresponding epoch averaged $S(\lambda)$ anomalies (see Figure 6) though. Nevertheless, both impacts have to be considered since the decrease of the correlation is height- and wavelength-dependent.
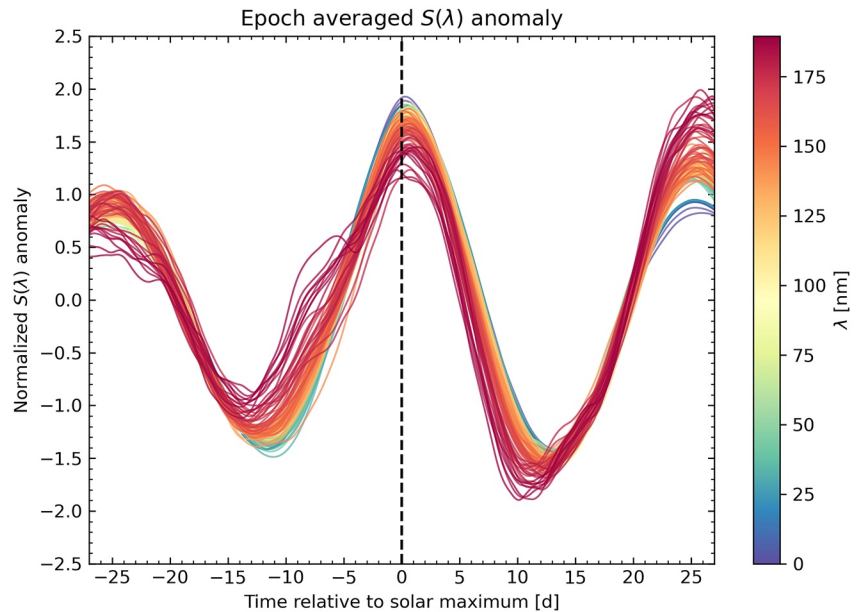
Figure 6. Superposed epoch analysis results for solar irradiance $S(\lambda)$. Each epoch averaged $S(\lambda)$ anomaly is colored coded according to the wavelength λ.

In terms of height, the correlation in Figure 7a is divided into two regions. Constant correlations are observed at heights from -20 to 20 km, which relates to the dominant O^+ at the N_e peak and 27-day signatures that are defined by the balance of O^+ production and loss. The accumulation of O^+ (and thus an increase of the delay) occurs at approximately 10 km (see Figure 7b). Better correlations are observed for the subregion above the N_e peak (from 10 to 20 km) compared to the subregion below (from -20 to 10 km). This difference is due to the stronger absorption of solar EUV radiation at greater heights in this region. Another region at heights from -100 to -20 km is defined by a continuous increase of the correlation toward lower heights. While the dominant O_2^+ at heights from -80 to -60 km defines a subregion that is driven by the O_2^+ production and loss (but also photo-dissociation), the subregion at heights from -60 to -20 km indicates likely a transition region. This transition
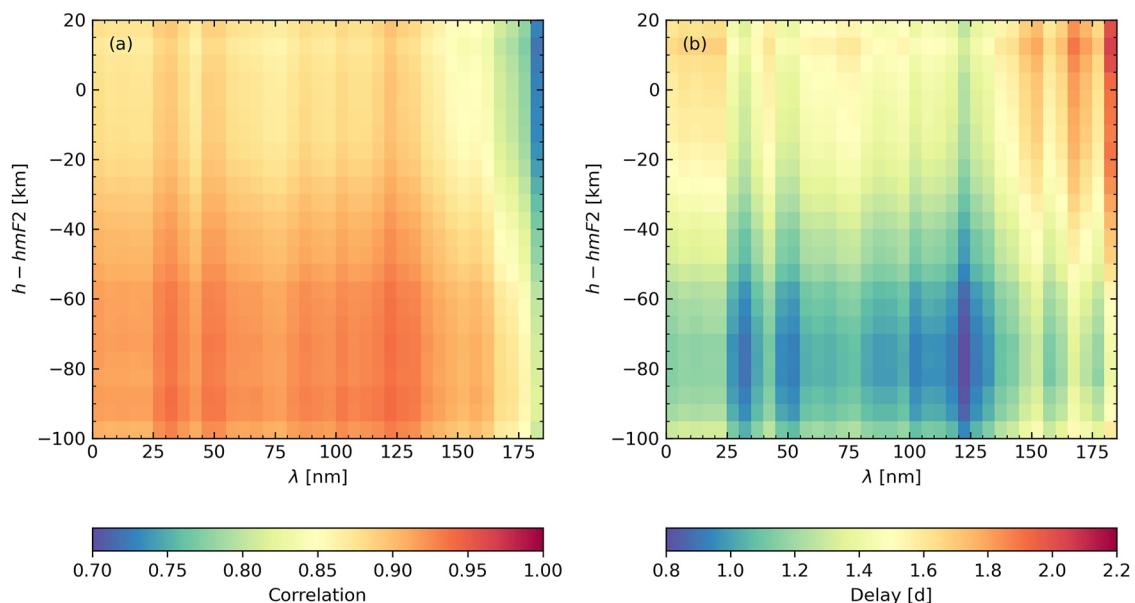

Figure 7. Correlation (a) and delay (b) from the cross-correlation analysis of epoch averaged solar irradiance $S(\lambda)$ and electron density $N_e(h_r)$ anomalies. The results are averaged to a grid of 5 nm × 5 km.

region, where processes related to both species, O and O_2, occur, is important to discuss the impact of transport processes (Schmölter et al., 2022), which in turn impact the composition and delayed ionospheric response. The transition between the two major species and related processes is also reflected with the increasing correlation at lower heights from −20 to −60 km and at wavelengths from 150 to 175 nm. This part of the UV spectrum is absorbed via photodissociation of O_2 (Kelley, 2009) and not photoionization.

The wavelength-dependent analysis of O and O_2 photoionization is difficult since their cross sections cover approximately the same part of the EUV spectrum (Fennelly & Torr, 1992) and since the epoch averaged $S(\lambda)$ anomaly amplitudes vary strongly for several spectral lines (e.g., Lyman-alpha line). There are increases of the correlation at wavelengths from 25 to 55 nm and from 80 to 135 nm, and especially for the lower ionosphere the second increase may be attributed to O_2 photoionization (Fennelly & Torr, 1992; Schmölter et al., 2022) due to the smallest delays that are observed for this region (see Figure 7b). The photodissociation of O_2 is identified through the height-dependent variations at wavelengths from 150 to 175 nm.

The delays in Figure 7b show stronger variations than the delays in Figure 5. In the lower ionosphere at heights from −100 to −60 km the delay is less than 1 day and especially at the Lyman-alpha line a significant decrease of the delay is observed. In the upper ionosphere at heights from −40 to −20 km longer delays are observed. Thus, the height-dependent delay variations are in good agreement with the results based on F10.7 anomalies in Figure 5.

Figure 8 shows the mean values of $S(\lambda)$ and $\tau(\lambda)$ over all heights. The correlation between $S(\lambda)$ in Figure 8a and the running mean of $\tau(\lambda)$ in Figure 8d is 0.11, and for this reason the wavelength-dependent solar irradiance amplitude has no significant impact on the estimated delays. The delayed ionospheric response is controlled by the major absorption processes which in turn interact with the neutral and ionized composition. The total ionization cross sections σ_A of O and O_2 are shown in Figures 8b and a sum of both cross sections is represented by the black line. Neither $S(\lambda)$ nor $\sigma_A(\lambda)$ are correlated with $\tau(\lambda)$, since complex interactions resulting from the initial absorption processes control the observed 27-day signatures. The importance of these interactions is further confirmed by a more comprehensive analysis of the energy deposition q_E (see Figure 8c) according to

$$q_E(\lambda, h_r) = n_O(h_r) \cdot \sigma_{A,O}(\lambda) \cdot S(\lambda) \cdot e^{-o(\lambda, h_r)} + n_{O_2}(h_r) \cdot \sigma_{A,O_2}(\lambda) \cdot S(\lambda) \cdot e^{-o(\lambda, h_r)}. \qquad (2)$$

This approach combines $S(\lambda)$ and $\sigma_A(\lambda)$ to estimate the impact of the direct absorption on $\tau(\lambda)$. However, the neutral densities, n_O and n_{O_2}, are simplified via logarithmic functions and the geometry of the ionosphere, which would be calculated as part of the optical depth $o(\lambda, h_r)$ using the Chapman function, is neglected. The weak correlation of 0.41 between $q_E(\lambda)$ and $\tau(\lambda)$ is increased compared to the correlation between $S(\lambda)$ and $\tau(\lambda)$, but also reflects no significant relation with the delay. Thus, the wavelength-dependent delayed ionospheric response can only be related to the solar EUV spectrum if further processes are considered (e.g., recombination, composition changes via photodissociation, and transport processes) and comprehensive ionosphere modeling using solar EUV measurements is performed.

The results in Figure 8 are particularly interesting with respect to previous studies that were able to show a correlation between total solar activity (e.g., F10.7) and delay using different approaches (Schmölter et al., 2020; Vaishnav et al., 2021). Thus, a wavelength- and height-dependent analysis using an even larger data set (large enough for selection of different solar activities with enough samples for the SEA technique) with appropriate modeling may investigate the relation in more detail in the future.

5. Height-Dependent Lag Analysis of O_2 Density Profiles

Results in previous studies (e.g., Ren et al., 2018; Schmölter et al., 2022) and the present analysis (see Figures 5 and 7) show the importance of the neutral composition for the delayed ionospheric response. Especially the O_2 density distribution is of interest, since the interaction of solar EUV with this species may increase (photodissociation) or decrease (recombination) the delayed ionospheric response that is observed at the N_e peak. For this reason, the SEA technique is further applied to O_2 density profiles provided through GOLD occultation measurements. The location of each O_2 density profile depends on the trace toward the limb and thus the measurements are distributed over both limbs (see Figure 9). A sufficient time series of O_2 density profiles is extracted from the data set by defining a region (black box from 129°W to 127°W and from 24°S to 5°S in Figure 9) that includes enough measurements but is also limited to a specific region.
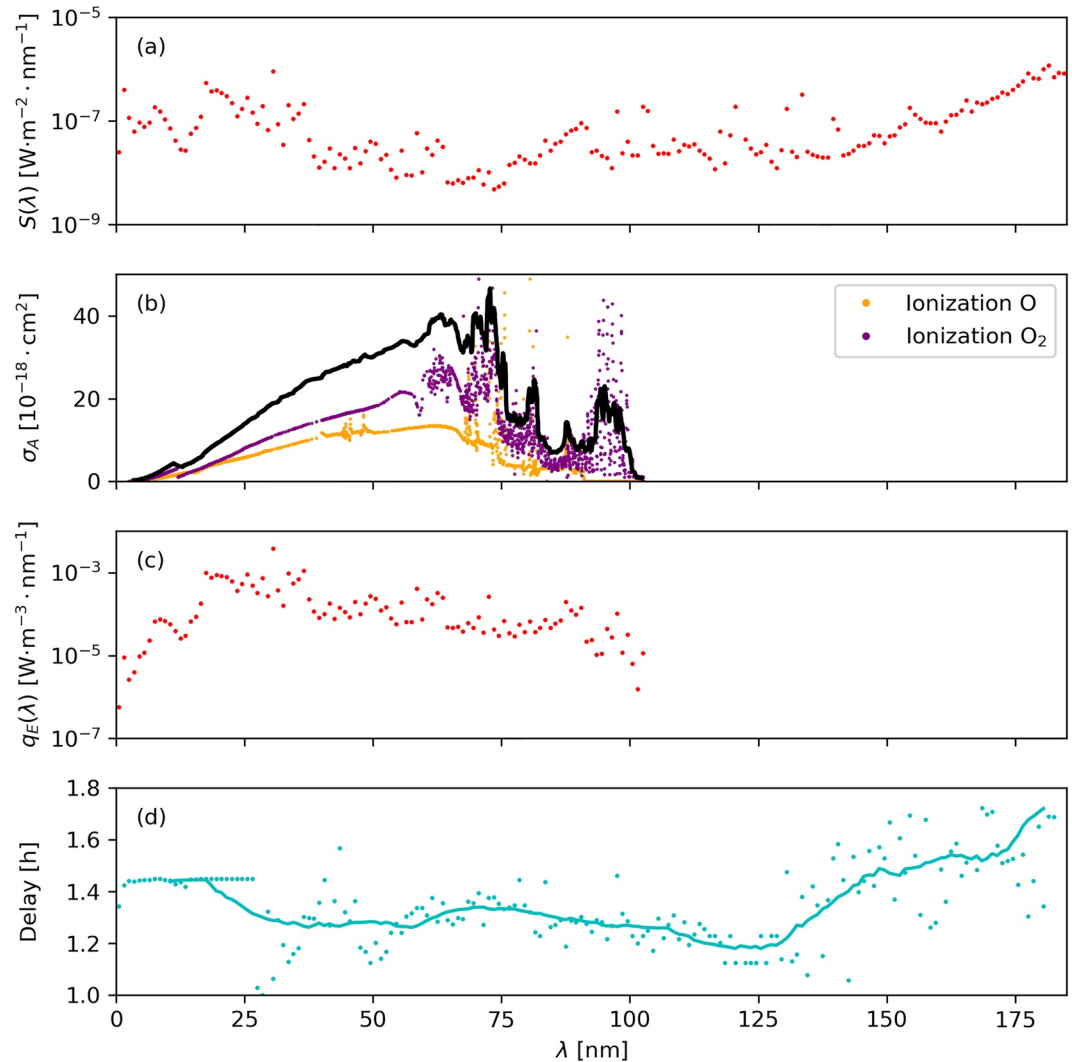
Figure 8. Mean solar irradiance $S(\lambda)$ for all selected epochs (a), ionization cross section σ_A (b), energy deposition q_E (c) and delay (d). A running mean with a window of 20 nm is shown for the delay with the solid line. The ionization cross section σ_A of O (orange dots) and O_2 (purple dots) according to Fennelly and Torr (1992) are shown (b). The sum of the cross sections (black line) is smoothed with a running mean.

The extracted O_2 density profiles are shown in Figure 10. There are several restrictions with the extracted data set that have to be considered for the significance of applied analysis. The available period with data is shorter, which reduces the number of epoch centers for the SEA technique (see black dots in Figure 10). Additionally, there are more data gaps throughout the period and therefore interpolation has to be applied more frequently (limited to 5% for selected epochs though). The observed F10.7 anomalies are also less significant compared to the observed amplitudes in Figure 2 and for that reason maxima greater than 1.5 sfu are included. Nevertheless, the O_2 density profiles in Figure 10 indicate variability (e.g., annual and seasonal variation), and 18 epochs according to the F10.7 anomalies are extracted (2 epochs are removed manually due to overlap).

The epoch averaged F10.7 and $n_{O_2}(150\ km)$ anomalies are shown in Figure 11. The lower number of epochs also affects the epoch averaged F10.7 anomaly with significant deviations compared to a sinusoidal fit. Nevertheless, a pronounced 27-day signature is extracted. The epoch averaged $n_{O_2}(150\ km)$ anomaly is even stronger affected by deviations, but nevertheless a variation representing a 27-day signature is extracted as well. The Monte-Carlo significance test estimates a fraction of 7.68% for $n_{O_2}(150\ km)$ and thus the significance is an order of magnitude smaller compared to the results based on N_e profiles (see Figure 3). At the upper boundary (250 km) the fractions increase, which may be attributed to data gaps and the smaller number of epochs, but the decreasing n_{O_2} may
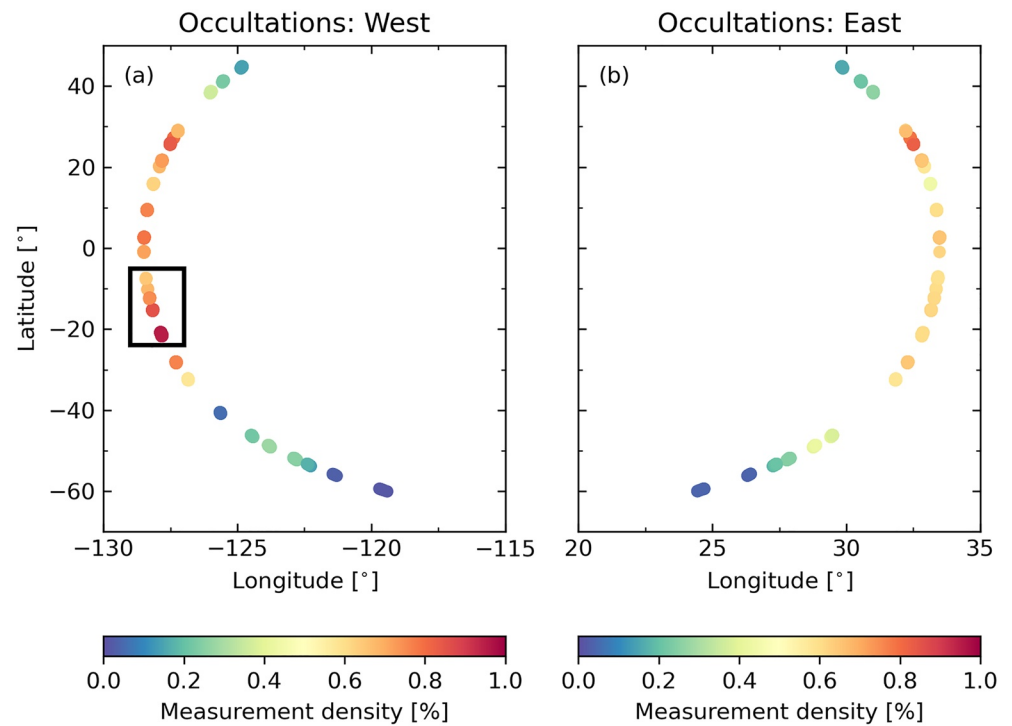
Figure 9. Location of O_2 density profiles from Global-scale Observations of the Limb and Disk occultation measurements. The black box from 129°W to 127°W and from 24°S to 5°S marks the data selection that is used in the further analysis. The density distribution of measurements is shown relative to the total number of measurements.

also explain a less pronounced response to solar activity. At the lower boundary (120 km) the fraction increase strongly up to 90% due to data gaps and the smaller number of epochs. These heights are not included in the further analysis and thus a mean fraction of 10.10% is observed.

Figure 12 shows the epoch averaged n_{O_2} anomalies at heights from 115 to 250 km. The exponential decrease of n_{O_2} with heights is accounted for by dividing $n_{O_2}(h)$ by the mean at each height. Thus, the relative rather than the absolute variation is shown in Figure 12b. Both, results in Figures 11 and 12, show a negative delay (left shift) of
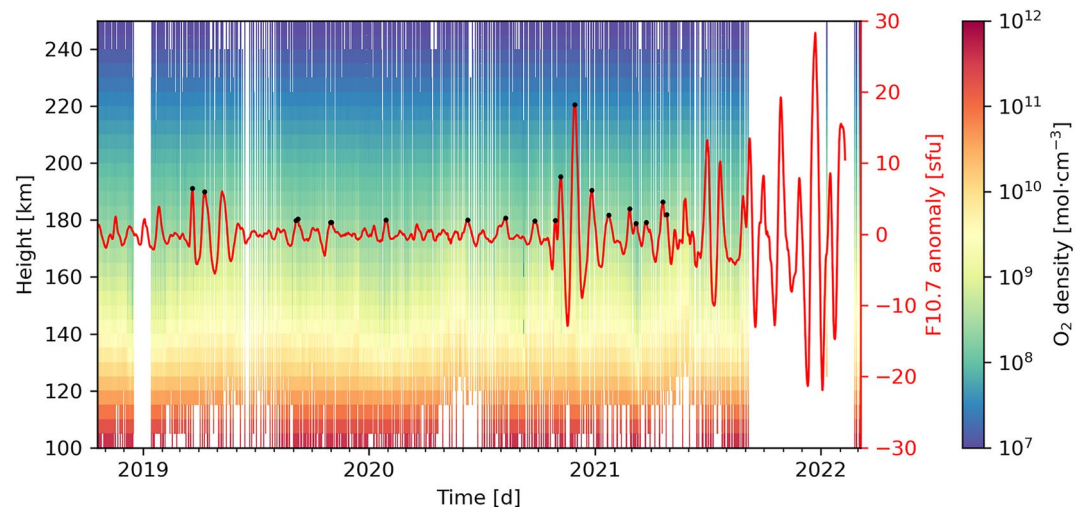

Figure 10. O_2 density profiles from 2019 to 2022 from Global-scale Observations of the Limb and Disk occultation measurements. Anomaly time series of F10.7 (red line), and identified F10.7 maxima (i.e., the epoch centers) are shown as black dots. Only F10.7 maxima greater than 1.5 sfu are included.
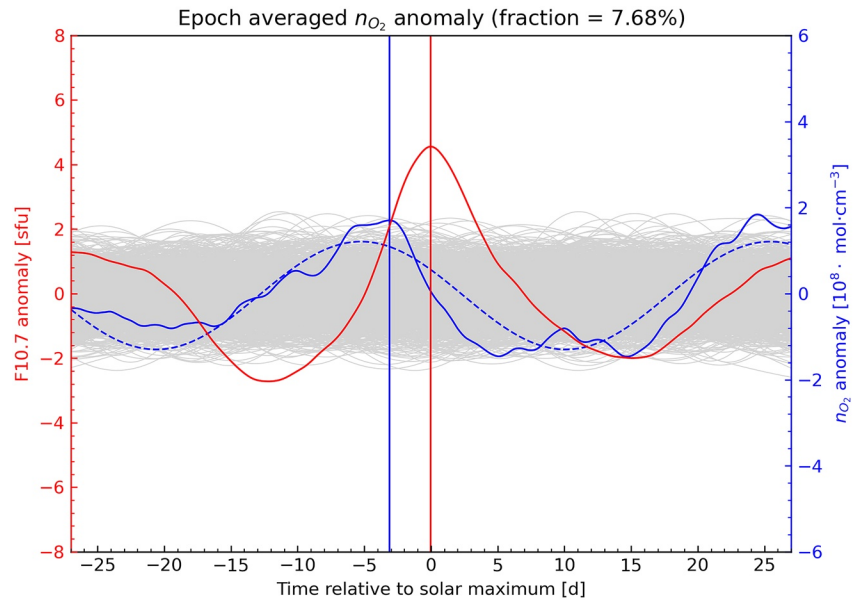
Figure 11. Superposed epoch analysis (SEA) results for F10.7 (red line) and O_2 density at the height of 150 km (blue line). The vertical lines mark the corresponding peak maxima. The dashed blue line shows the sinusoidal fit for the $n_{O_2}(150 \text{ km})$ SEA. The gray lines are a sample result of the Monte-Carlo significance test for $n_{O_2}(150 \text{ km})$.

the 27-day signatures that decreases at lower heights. This is in good agreement with TIE-GCM simulations by Schmölter et al. (2022) using an artificial sinusoidal solar input. The strongest change of n_{O_2} is observed at heights from 130 to 180 km with delays of approximately −7 to −3 days. The delay decreases further at lower heights up to −10 days. Furthermore, such a strong shift compared to the solar 27-day signature indicates a relation to similar delays that have been reported for middle atmosphere parameters, for example, a delay of 13 days observed for tropical upper mesospheric O by Lednyts'kyy et al. (2017). The observed delays in the lower ionosphere/ thermosphere and mesosphere may be related due to propagation via transport processes (Schmölter et al., 2022; Vincent, 2015).
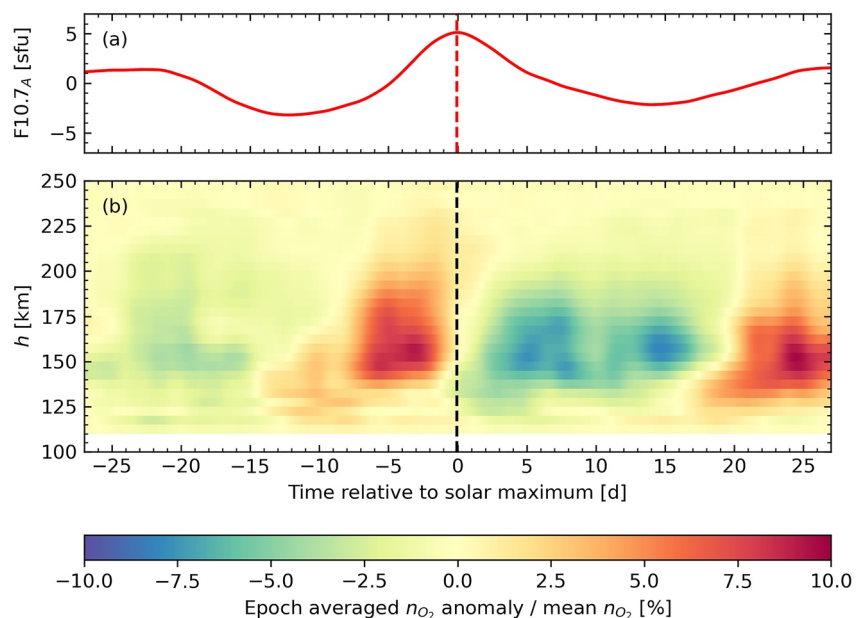

Figure 12. Superposed epoch analysis results for F10.7 (a) and O_2 density (relative to mean O_2 density) at heights from 115 to 250 km (b).
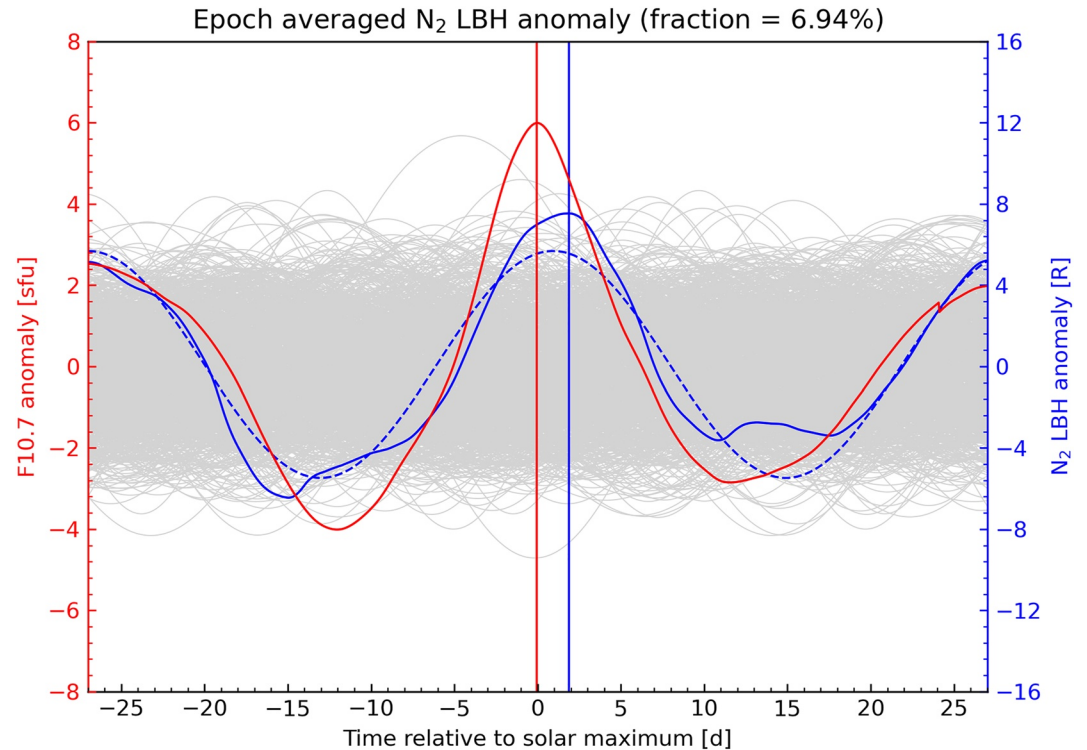
Figure 13. Superposed epoch analysis (SEA) results for F10.7 (red line) and N$_2$ Lyman-Birge-Hopfield (LBH) radiance (blue line). The vertical lines mark the corresponding peak maxima. The dashed blue line shows the sinusoidal fit for the N$_2$ LBH radiance SEA. The gray lines are a sample result of the Monte-Carlo significance test for N$_2$ LBH radiance.

The SEA technique applied to GOLD O$_2$ density profiles is limited due to the discussed restrictions, but the retrieved variations of the delayed response are in good agreement with previous studies (Schmölter et al., 2022). For this reason, the results provide further insight to the change of the neutral composition during the 27-day solar rotation period. The analysis may be extended in future studies when longer periods of GOLD measurements are available.

6. Lag Analysis of N$_2$ LBH Radiance

Schmölter et al. (2021) investigated two 27-day solar rotation periods with different ionospheric and thermospheric parameters including GOLD O/N$_2$ measurements. While the periods indicated some relation with long-term variations (greater than 27 days), no correlation with the 27-day solar rotation period was observed due significant short-term variations (smaller than 27 days). The observed variations may be due to processes in the upper atmosphere, for example, temperature, density, or wind changes caused by atmospheric waves (He et al., 2010), or due to the higher sensitivity of the ratio to changes in general (Schmölter et al., 2021).

The SEA technique applied to GOLD O/N$_2$ column density ratio confirms these results since no well-defined epoch averaged anomaly is estimated. But the analysis of the N$_2$ LBH radiance in Figure 13 extracts a significant response (similar fraction as in Figure 11). Since the N$_2$ LBH radiance is calculated from daytime disk scans and not occultation measurements, the analyzed region is adjusted in longitude (from 50°W to 48°W and from 24°S to 5°S) and no height profile is available. The calculated N$_2$ LBH radiance signature is in good agreement with the N_e signature (see Figure 3) and simulations of the delayed ionospheric response (Ren et al., 2018; Schmölter et al., 2022). In this sense, the results reflect the N_e balance (quasi-equilibrium), which is controlled by recombination via N$_2$ and O$_2$ (loss coefficients k' and k'') in addition to the production via O (Rishbeth, 1998) as

$$N_e \sim \frac{I \cdot n_O}{k' \cdot n_{N_2} + k'' \cdot n_{O_2}}. \tag{3}$$

The solar flux I introduces the 27-day signature, which is correlated for N_e and n_{N_2} with similar delays (see Figures 3 and 13). Thus, there is no significant imbalance between the corresponding ionization and recombination

processes, that may contribute to the delayed ionospheric response. Contrary to this, N_e and n_{O_2} are correlated with significantly different delays (see Figures 3 and 11). Thus, this imbalance due to the enhanced loss of O_2 in the second phase of the 27-day solar rotation period (see Figure 12) driven by photodissociation causes an accumulation of O (increase n_O). N_e and n_{N_2} follow this increase (enhanced immediate production and loss) and a delayed ionospheric response is observed.

The results calculated from N_2 LBH radiance further indicate that the analysis of O_2 density distribution is important to characterize the delayed ionospheric response. SEA of OI 135.6 nm radiance and O/N_2 column density ratio would be of interest to confirm the results, but for both data sets no significant 27-day signatures can be extracted.

7. Discussion

7.1. Delay Estimation via the SEA Approach

The delayed ionospheric response estimated from F10.7 and $N_e(h_r)$ anomalies in Figure 5 is greater than results in previous studies (e.g., Schmölter et al., 2021) which is related to the epoch averaging as part of the SEA technique (smoother peaks), but also is caused by the inclusion of several anomalies during high solar activity. The delayed ionospheric response increases with solar activity (Schmölter et al., 2020) and strongly pronounced anomalies (increased solar activity due to 27-day solar rotation period) are well-suited for the SEA technique. Thus, a bias to greater delays is introduced due to the epoch center selection. The delay analysis in Figure 7 using $S(\lambda)$ and $N_e(h_r)$ anomalies is similarly affected.

The detection of epoch centers for the SEA technique based on F10.7 anomalies allows to define a general selection of 27-day signatures. The selection of $S(\lambda)$ anomalies based on these epoch centers shows that the solar EUV spectrum is correlated (especially the difference between adjacent 27-signatures is small), but, for example, the maxima in Figure 6 occur at different times relative to the solar maximum in F10.7. Additionally, the wavelength-dependent amplitude has to be considered because of its dominant impact on major absorption processes (see Equation 2 and Figure 8). This impact can only be addressed by appropriate ionospheric modeling and cannot be reflected via the statistical analysis of the delayed ionospheric response (peak comparison or cross-correlation).

7.2. 27-Day Signatures in Electron and O_2 Density

The extracted 27-day signatures in N_e and nO_2 are calculated from data sets that cover different time periods and refer to different geographic locations. The SEA approach should minimize the impact of these differences, but future investigations should aim for an analysis of data sets, that share a geographic location.

The relative heights, which have been applied for the N_e analysis, may be transformed to absolute heights for a direct comparison of the calculated delays. For this purpose, the mean height of the N_e peaks (at epoch centers) is added to the relative heights h_r according to

$$h = h_r + \overline{hmF2}. \tag{4}$$

Thus, h_r in Figure 5b would be adjusted to h by adding 253 km. The delays, τ_{N_e} and τ_{O_2}, are shown in Figure 14. The initial comparison between both delay series (cyan and magenta dots in Figure 14a) is moderately correlated (value of 0.65), but adding a manually selected correction of +10 km (in Equation 4) results in a strong correlation between τ_{N_e} and τ_{O_2} at heights from 150 to 250 km. This correlation of 0.91 (see Figure 14c) confirms, that O_2 and O_2^+ have a major impact on the delayed ionospheric response in the lower ionosphere, and the observed relation is in good agreement with TIE-GCM simulations by Schmölter et al. (2022). The observed significance for both, τ_{N_e} and τ_{O_2}, has to be considered for the results (especially τ_{O_2}), but the understanding of major absorption processes (Kelley, 2009) and studies of the delayed ionospheric response (e.g., Jakowski et al., 1991; Ren et al., 2018; Schmölter et al., 2022) support the relation shown in Figure 14. The difference between the τ_{N_e} and τ_{O_2} of several days is due their inverse relation according to the quasi-equilibrium (see Equation 3), which is controlled by ionization and recombination processes and further impacted by photodissociation.

If significantly longer periods of GOLD O_2 density measurements are available, the analysis performed in the present study could be extended. The SEA technique may be applied to a larger number of epochs to check whether
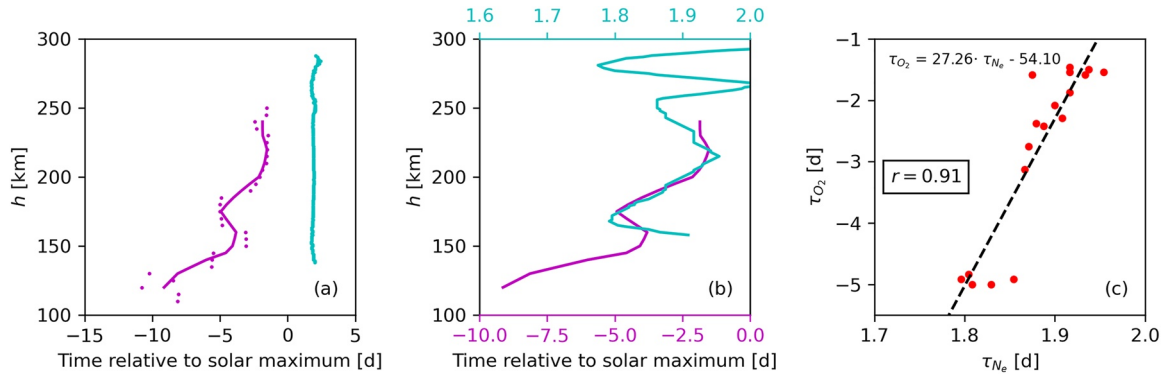
Figure 14. Panel (a) shows the delay between epoch averaged F10.7 and $N_e(h)$ anomalies (cyan dots) and the delay between epoch averaged F10.7 and $n_{O_2}(h)$ anomalies (magenta dots). The corresponding lines show a running mean with a window of 5 km for each data set. Panel (b) shows the same running means with separate scales for the time relative to the solar maximum. Panel (c) shows the correlation between both delay series (τ_{N_e} and τ_{O_2}) and the corresponding regression line.

an improvement for the significance and changes for the delay occur. Highly significant height-dependent results for epoch averaged N_e and n_{O_2} anomalies would further allow to calculate n_O anomalies (difference at greater heights), which would be of interest for studies of the ionospheric composition.

8. Conclusions

The present study extends the investigation by Schmölter et al. (2022) to a wavelength- and height-dependent SEA and thus calculates statistically significant 27-day signatures and delays from different solar and ionospheric/thermospheric data sets. For this reason, in comparison to previous studies, processes in the lower and upper ionosphere are discussed (without limitations due to low correlations). The SEA and delayed ionospheric response calculated from F10.7 and ionosonde (station Pruhonice) measurements (see Figures 4 and 5) confirm the results of previous studies (e.g., Jakowski et al., 1991; Ren et al., 2018; Schmölter et al., 2022). A maximum of the delay is observed at the N_e peak (dominated by O^+), which is related to accumulation of O^+ due to the imbalance of production and loss. A minimum of the delay is observed approximately 80 km below the N_e peak (dominated by O_2^+), which is related to the composition changing in favor of O via photodissociation of O_2 during the maximum of the 27-day solar rotation period. Thus, the production of O_2^+ decreases several days before production of O^+. The transition region between n_{O^+} and $n_{O_2^+}$ peaks shows an increase of the delay with height. The analysis is extended using wavelength-dependent solar irradiance measurements (see Figures 6 and 7) allowing to calculate wavelength- and height-dependent delays, which further show the impact of photoionization and photodissociation.

The SEA approach is also applied to O_2 density measurements showing the variability of corresponding 27-day signatures (see Figure 12). The results are in good agreement with TIE-GCM simulations by Schmölter et al. (2022) and support the discussed change of the neutral composition (in favor of O) during the first phase of the 27-day solar rotation period. The good agreement with previous studies and the significance of the results is further reflected by the strong correlation between the delayed response of N_e and n_{O_2} below 250 km (see Figure 14).

The mean and maximum delays between epoch averaged F10.7 and N_e anomalies as well as epoch averaged F10.7 and n_{O_2} anomalies are summarized in Table 1. The fractions calculated from the Monte-Carlo significance test, which are also shown in Table 1, indicate that the N_e anomalies (and the corresponding delays) are strongly driven by the solar activity at all heights. The significance for n_{O_2} anomalies is smaller, but the good agreement with the understanding of major absorption processes (Kelley, 2009) and studies of the delayed ionospheric response (e.g., Schmölter et al., 2022) indicate that the height-dependent variations of the delay are still correctly represented.

Future studies could extend the analysis to longer periods and may include different ionosonde stations. This would allow to define spatial and temporal

Table 1
Mean and Maximum Delay Between Epoch Averaged F10.7 and N_e Anomalies As Well As Epoch Averaged F10.7 and n_{O_2} Anomalies

	F10.7 and N_e	F10.7 and N_e	F10.7 and n_{O_2}	F10.7 and n_{O_2}
Parameter	Mean	Maximum	Mean	Maximum
dt_{max}	1.9 days	2.4 days	−4.0 days	−10.8 days
τ_{CC}	1.8 days	2.1 days	−2.8 days	−10.0 days
Fraction	0.10%	0.61%	10.10%	18.89%

Note. Delays are estimated using the time difference between peak maxima dt_{max} and the cross-correlation lag τ_{CC}. The fraction is calculated from the Monte-Carlo significance test. The mean and maximum are calculated over all available heights.

variations of the delayed ionospheric response. Additionally, the 27-day signatures during different solar and geomagnetic activity could be studied if a sufficient amount of epochs for various conditions is available.

Data Availability Statement

The OMNI data were obtained from the GSFC/SPDF OMNIWeb interface at https://omniweb.gsfc.nasa.gov/. The TIMED/SEE data were obtained from the LASP web interface at https://lasp.colorado.edu/home/see/data/. The ionosonde data were obtained from the NOAA NCEI repository at https://ngdc.noaa.gov/stp/iono/grams.html. The GOLD data were obtained from the NASA web interface at https://gold.cs.ucf.edu/data/.

References

Afraimovich, E. L., Astafyeva, E. I., Oinats, A. V., Yasukevich, Y. V., & Zhivetiev, I. V. (2008). Global electron content: A new conception to track solar activity. *Annales Geophysicae*, *26*(2), 335–344. https://doi.org/10.5194/angeo-26-335-2008

Cai, X., Burns, A. G., Wang, W., Qian, L., Solomon, S. C., Eastes, R. W., et al. (2021). Investigation of a neutral "tongue" observed by GOLD during the geomagnetic storm on May 11, 2019. *Journal of Geophysical Research: Space Physics*, *126*(6), e2020JA028817. https://doi.org/10.1029/2020ja028817

CAS. (2022). Institute of atmospheric physics, průhonice ionospheric station. Retrieved from https://www.ufa.cas.cz/en/institute-structure/department-of-ionosphere-and-aeronomy/pruhonice-ionospheric-station/

Eastes, R. W., McClintock, W. E., Burns, A. G., Anderson, D. N., Andersson, L., Aryal, S., et al. (2020). Initial observations by the GOLD mission. *Journal of Geophysical Research: Space Physics*, *125*(7). https://doi.org/10.1029/2020ja027823

Eastes, R. W., McClintock, W. E., Burns, A. G., Anderson, D. N., Andersson, L., Codrescu, M., et al. (2017). The global-scale observations of the limb and disk (GOLD) mission. *Space Science Reviews*, *212*(1–2), 383–408. https://doi.org/10.1007/s11214-017-0392-2

Fennelly, J., & Torr, D. (1992). Photoionization and photoabsorption cross sections of O, N_2, O_2, and N for aeronomic calculations. *Atomic Data and Nuclear Data Tables*, *51*(2), 321–363. https://doi.org/10.1016/0092-640x(92)90004-2

He, M., Liu, L., Wan, W., Lei, J., & Zhao, B. (2010). Longitudinal modulation of the O/N_2 column density retrieved from TIMED/GUVI measurement. *Geophysical Research Letters*, *37*(20). https://doi.org/10.1029/2010gl045105

Jakowski, N., Fichtelmann, B., & Jungstand, A. (1991). Solar activity control of ionospheric and thermospheric processes. *Journal of Atmospheric and Terrestrial Physics*, *53*(11), 1125–1130. (The 7th International Scostep symposium on Solar-Terrestrial Physics). https://doi.org/10.1016/0021-9169(91)90061-B

Jakowski, N., Heise, S., Wehrenpfennig, A., Schlüter, S., & Reimer, R. (2002). GPS/GLONASS-based TEC measurements as a contributor for space weather forecast. *Journal of Atmospheric and Solar-Terrestrial Physics*, *64*(5–6), 729–735. https://doi.org/10.1016/s1364-6826(02)00034-2

Kamal, S., Jakowski, N., Hoque, M. M., & Wickert, J. (2020). Evaluation of E layer dominated ionosphere events using COSMIC/FORMOSAT-3 and CHAMP ionospheric radio occultation data. *Remote Sensing*, *12*(2), 333. https://doi.org/10.3390/rs12020333

Kelley, M. (2009). *The Earth's ionosphere* (Vol. 96). Academic Press. https://doi.org/10.1016/B978-0-12-404013-7.X5001-1

LASP. (2022). Home page of the solar EUV experiment (SEE). Retrieved from https://lasp.colorado.edu/home/see/data/

Lednyts'kyy, O., von Savigny, C., & Weber, M. (2017). Sensitivity of equatorial atomic oxygen in the MLT region to the 11-year and 27-day solar cycles. *Journal of Atmospheric and Solar-Terrestrial Physics*, *162*, 136–150. https://doi.org/10.1016/j.jastp.2016.11.003

Lee, C.-K., Han, S.-C., Bilitza, D., & Seo, K.-W. (2012). Global characteristics of the correlation and time lag between solar and ionospheric parameters in the 27-day period. *Journal of Atmospheric and Solar-Terrestrial Physics*, *77*, 219–224. https://doi.org/10.1016/j.jastp.2012.01.010

Lumpe, J. D., McClintock, W. E., Evans, J. S., Correira, J., Veibell, V., Beland, S., & Eastes, R. (2020). A new data set of thermospheric molecular oxygen from the global-scale observations of the limb and disk (GOLD) mission. *Journal of Geophysical Research: Space Physics*, *125*(4). https://doi.org/10.1029/2020ja027812

Ma, R., Xu, J., Wang, W., & Lei, J. (2012). The effect of ~27 day solar rotation on ionospheric F2 region peak densities (NmF2). *Journal of Geophysical Research*, *117*(A3). https://doi.org/10.1029/2011ja017190

Min, K., Park, J., Kim, H., Kim, V., Kil, H., Lee, J., et al. (2009). The 27-day modulation of the low-latitude ionosphere during a solar maximum. *Journal of Geophysical Research*, *114*(A4), A04317. https://doi.org/10.1029/2008JA013881

NASA. (2022a). Global-scale observations of the limb and disk - data. Retrieved from https://gold.cs.ucf.edu/data/

NASA. (2022b). NASA/GSFC's OMNIWeb interface. Retrieved from https://omniweb.gsfc.nasa.gov/form/dx1.html

NCEI. (2022). Vertical ionograms. Retrieved from https://data.ngdc.noaa.gov/instruments/remote-sensing/active/profilers-sounders/ionosonde/data/

Oinats, A. V., Ratovsky, K. G., & Kotovich, G. V. (2008). Influence of the 27-day solar flux variations on the ionosphere parameters measured at Irkutsk in 2003–2005. *Advances in Space Research*, *42*(4), 639–644. https://doi.org/10.1016/j.asr.2008.02.009

Ren, D., Lei, J., Wang, W., Burns, A., Luan, X., & Dou, X. (2018). Does the peak response of the ionospheric F 2 region plasma lag the peak of 27-day solar flux variation by multiple days? *Journal of Geophysical Research: Space Physics*, *123*(9), 7906–7916. https://doi.org/10.1029/2018JA025835

Ren, D., Lei, J., Wang, W., Burns, A., Luan, X., & Dou, X. (2019). A simulation study on the time delay of daytime thermospheric temperature response to the 27-day solar EUV flux variation. *Journal of Geophysical Research: Space Physics*, *124*(11), 9184–9193. https://doi.org/10.1029/2019ja027000

Ren, D., Lei, J., Wang, W., Burns, A., Luan, X., & Dou, X. (2020). Different peak response time of daytime thermospheric neutral species to the 27-day solar EUV flux variations. *Journal of Geophysical Research: Space Physics*, *125*(7), e2020JA027840. https://doi.org/10.1029/2020ja027840

Rishbeth, H. (1998). How the thermospheric circulation affects the ionospheric F2-layer. *Journal of Atmospheric and Solar-Terrestrial Physics*, *60*(14), 1385–1402. https://doi.org/10.1016/S1364-6826(98)00062-5

Rishbeth, H., & Mendillo, M. (2001). Patterns of F2-layer variability. *Journal of Atmospheric and Solar-Terrestrial Physics*, *63*(15), 1661–1680. https://doi.org/10.1016/S1364-6826(01)00036-0

Rong, P., von Savigny, C., Zhang, C., Hoffmann, C. G., & Schwartz, M. J. (2020). Response of middle atmospheric temperature to the 27 d solar cycle: An analysis of 13 years of microwave limb sounder data. *Atmospheric Chemistry and Physics*, *20*(3), 1737–1755. https://doi.org/10.5194/acp-20-1737-2020

Schmölter, E., Berdermann, J., & Codrescu, M. (2021). The delayed ionospheric response to the 27-day solar rotation period analyzed with GOLD and IGS TEC data. *Journal of Geophysical Research: Space Physics*, *126*(2), e2020JA028861. https://doi.org/10.1029/2020ja028861

Schmölter, E., Berdermann, J., Jakowski, N., & Jacobi, C. (2020). Spatial and seasonal effects on the delayed ionospheric response to solar EUV changes. *Annales Geophysicae*, *38*(1), 149–162. https://doi.org/10.5194/angeo-38-149-2020

Schmölter, E., Berdermann, J., Jakowski, N., Jacobi, C., & Vaishnav, R. (2018). Delayed response of the ionosphere to solar EUV variability. *Advances in Radio Science*, *16*, 149–155. https://doi.org/10.5194/ars-16-149-2018

Schmölter, E., Heymann, F., Savigny, C., & Berdermann, J. (2022). The height-dependent delayed ionospheric response to solar EUV. *Journal of Geophysical Research: Space Physics*, *127*(3), e2021JA030118. https://doi.org/10.1029/2021ja030118

Strickland, D. J., Evans, J. S., & Paxton, L. J. (1995). Satellite remote sensing of thermospheric O/N2 and solar EUV: 1. Theory. *Journal of Geophysical Research*, *100*(A7), 12217. https://doi.org/10.1029/95ja00574

Tapping, K. F. (2013). The 10.7 cm solar radio flux (F10.7). *Space Weather*, *11*(7), 394–406. https://doi.org/10.1002/swe.20064

Titheridge, J. E. (1973). The electron content of the southern mid-latitude ionosphere, 1965–1971. *Journal of Atmospheric and Terrestrial Physics*, *35*(5), 981–1001. https://doi.org/10.1016/0021-9169(73)90077-9

Vaishnav, R., Jacobi, C., & Berdermann, J. (2019). Long-term trends in the ionospheric response to solar extreme-ultraviolet variations. *Annales Geophysicae*, *37*(6), 1141–1159. https://doi.org/10.5194/angeo-37-1141-2019

Vaishnav, R., Jacobi, C., Berdermann, J., Codrescu, M., & Schmölter, E. (2021). Role of eddy diffusion in the delayed ionospheric response to solar flux changes. *Annales Geophysicae*, *39*(4), 641–655. https://doi.org/10.5194/angeo-39-641-2021

Vaishnav, R., Jacobi, C., Berdermann, J., Schmölter, E., & Codrescu, M. (2018). Ionospheric response to solar EUV variations: Preliminary results. *Advances in Radio Science*, *16*, 157–165. https://doi.org/10.5194/ars-16-157-2018

Vincent, R. A. (2015). The dynamics of the mesosphere and lower thermosphere: A brief review. *Progress in Earth and Planetary Science*, *2*(1), 4. https://doi.org/10.1186/s40645-015-0035-8

von Savigny, C., Peters, D. H. W., & Entzian, G. (2019). Solar 27-day signatures in standard phase height measurements above central Europe. *Atmospheric Chemistry and Physics*, *19*(3), 2079–2093. https://doi.org/10.5194/acp-19-2079-2019

Woods, T. N. (2005). Solar EUV Experiment (SEE): Mission overview and first results. *Journal of Geophysical Research*, *110*(A1), A01312. https://doi.org/10.1029/2004ja010765

Woods, T. N., Bailey, S., Eparvier, F., Lawrence, G., Lean, J., McClintock, B., et al. (2000). TIMED solar EUV experiment. *Physics and Chemistry of the Earth - Part C: Solar, Terrestrial & Planetary Science*, *25*(5–6), 393–396. https://doi.org/10.1016/s1464-1917(00)00040-4

Woods, T. N., Bailey, S. M., Eparvier, F. G., Lawrence, G. M., Lean, J., McClintock, W. E., et al. (1998). TIMED solar EUV experiment. In C. M. Korendyke (Ed.), *SPIE proceedings* (pp. 180–191). SPIE. https://doi.org/10.1117/12.330255

Zhang, S.-R., & Holt, J. M. (2008). Ionospheric variability from an incoherent scatter radar long-duration experiment at Millstone Hill. *Journal of Geophysical Research*, *113*(A3). https://doi.org/10.1029/2007ja012639